Computers and Concrete, *Vol. 16, No. 4 (2015) 587-604*
DOI: http://dx.doi.org/10.12989/cac.2015.16.4.587

Discrete crack analysis for concrete structures using the hybrid-type penalty method

Yoshihiro Fujiwara[*1], Norio Takeuchi[1a], Tadahiko Shiomi[2b] and Atsushi Kambayashi[3c]

[1]*Graduate School of Engineering and Design, Hosei University, 2-33 Ichigaya Tamachi, Shinjuku, Tokyo 162-0843, Japan*
[2]*Mind Inc., 7-17-19 Maebara-nishi Funabashi Chiba 274-0825, Japan*
[3]*Research & Development Institute, Takenaka Corporation, 1-5-1 Ohtsuka, Inzai, Chiba 270-1395, Japan*

(Received February 28, 2013, Revised January 15, 2015, Accepted October 22, 2015)

Abstract. The hybrid-type penalty method (HPM) is suitable for representing failure phenomena occurring during the transition from continua to discontinua in materials such as concrete. Initiation and propagation of dominant cracks and branching of cracks can easily be modeled as a discrete crack. The HPM represents a discrete crack by eliminating the penalty that represents the separation of the elements at the intersection boundary. This treatment is easy because no change in the degrees of freedom for the discrete crack is necessary. In addition, it is important to evaluate the correct deformation of the continua before the crack formation is initiated. To achieve this, we implemented a constitutive model of concrete for the HPM. In this paper, we explain the implemented constitutive model and describe the simulation of an anchor bolt pullout test using the HPM demonstrating its capability for evaluating progressive failure.

Keywords: hybrid-type penalty method; discrete crack; concrete structure

1. Introduction

We are still dealing with significant damage to concrete structures due to recent large earthquakes. Therefore, it is important to understand the failure mechanism of concrete structures. A dominant crack is initiated in a concrete structure by tensile stress, and subsequently the crack grows, propagates, and branches until the structure finally collapses. To predict the progressive failure of a concrete structure, computation of a discrete crack is essential to evaluate the crack accurately. Computer simulation can predict crack growth, propagation, and branching leading to failure of the concrete structure.

The crack models for concrete are classified as the "smeared crack model" (e.g., Bazant and Oh 1983) and the "discrete crack model" (e.g., Barlenblatt 1962). The discrete crack model describes the actual crack well.

In the smeared crack model, it is difficult to describe an actual crack because the crack width is

*Corresponding author, Student, E-mail: fujiwara.yoshihiro@3d-lab.jp
[a]Professor, E-mail: takeuchi@hosei.ac.jp
[b]Engineering Director, E-mail: shiomi.tadahiko@3d-lab.jp
[c]Chief Engineer, E-mail: kanbayashi.atsushi@takenaka.co.jp

http://www.techno-press.org/?journal=cac&subpage=8 ISSN: 1598-8198 (Print), 1598-818X (Online)

represented by a large strain at Gaussian points. The precise concentrated stress around the crack tip does not appear even though it has an important role for crack propagation. Sato and Naganuma (2007) improved the model by using bond slips in the smeared crack context to evaluate crack width.

There are two approaches in the discrete crack model. One is separating elements at the intersection boundary to represent the crack. Miehe and Gürses (2007) introduced a discretization technique in terms of node doubling as the most natural setting for the brittle fracture problem. The other is the extended finite element method (XFEM) (Belytschko and Black 1999) which calculates a discrete crack by enriching the displacement interpolation with a discontinuous function based on the partition of unity concept. Many researchers have analyzed discrete cracks in a concrete specimen using XFEM (e.g., Unger *et al.* 2007, Theiner and Hofstetter 2009).

The particle method is one of the methods used to represent a discrete crack. It is suitable in qualitative analysis, such as when studying how to demolish a structure, but it is not accurate for quantitative analysis. Rabczuk and Belytschko (2007) analyzed cracks in a concrete structure by the particle method.

Another good method to represent a crack is to separate the intersection boundary in each elements. Before the initiation of a crack, the separated rigid bodies or elements are tied by spring elements or a penalty to represent a continuum. This tied condition is eliminated to represent crack initiation. The advantage of this method is its simplicity. There is no need for tracking the crack path.

The rigid body spring model (RBSM) developed by Kawai (1977) is a good method to calculate a discrete crack. In this method, a discrete crack is modeled by a spring located at the boundary of the elements. Separation of the continuum is easy to model by this method. Initially, it obtained good results for the problem of the strong nonlinearity of steel. It was then applied to discrete limit analysis of soils and concrete structures (Takeuchi *et al.* 2005). However, the elastic deformation in the continua obtained by RBSM is not accurate, because it models a continuum to connect the spring elements between the edges of the rigid bodies. RBSM is still used to model realistic behavior of concrete structures from cracking to failure (Gedik *et al.* 2011).

The hybrid-type penalty method (HPM), developed by Takeuchi *et al.* (2000), refined the RBSM method for calculating elastic deformation of the elements using the finite element method (FEM), and introduced a Lagrange multiplier to satisfy the subsidiary condition of continuous displacement in the hybrid-type virtual work formulation. The HPM is suited to analyzing progressive failure of concrete structures with the following features:

• Accurate deformation can be calculated before crack initiation because an elastic element (called a subdomain in HPM) is used. Even after crack initiation, it is important to calculate the correct deformation within the elastic area between cracks.

• The HPM models a discrete crack by eliminating the penalty that represents separation of the elements at the intersection boundary. This treatment is easy because no change in the degrees of freedom for a discrete crack is necessary.

• The concentrated stress at the crack tip can be calculated without the J-integral, which was developed by Rice (1968). The HPM makes it easy to obtain accurate concentrated stress around the crack using the correct relationship between tensile stress and the displacement of the crack mouth opening.

The authors implemented a constitutive model of concrete material in the original HPM to make it possible to compute progressive failure phenomena of a concrete structure. In the present paper, we introduce the basic formulation of the HPM and describe an implemented constitutive

model of concrete. We applied an empirical expression of the tension-softening curve in the constitutive model to represent correct deformation during crack opening. Finally, we validated the accuracy of the constitutive model by simulating a pullout test of an anchor bolt embedded in flat concrete.

2. Theory of HPM

2.1 Governing equation

The basic equation of the elastic problem is as follows

$$\operatorname{div} \boldsymbol{\sigma} + \boldsymbol{f} = 0 \quad \text{in } \Omega, \tag{1}$$

$$\boldsymbol{\sigma} = \boldsymbol{D} : \boldsymbol{\varepsilon}, \tag{2}$$

$$\boldsymbol{\varepsilon} = \boldsymbol{\nabla}^s \boldsymbol{u} \overset{\text{def.}}{=} \frac{1}{2}\left[\boldsymbol{\nabla u} + (\boldsymbol{\nabla u})^t\right], \tag{3}$$

where $\boldsymbol{\sigma}$ is the Cauchy stress tensor; $\boldsymbol{f}$, the body force per unit volume; $\boldsymbol{\varepsilon}$, the infinitesimal strain tensor; $\boldsymbol{D}$, the constitutive tensor; $\boldsymbol{\nabla}:=(\partial/\partial \boldsymbol{x}_i)\boldsymbol{e}_i$, the differential operator; $\boldsymbol{\nabla}^S$, the symmetric part of $\boldsymbol{\nabla}$; and $\boldsymbol{u}$, the displacement field in $\boldsymbol{x} \in \Omega$, Ω is the reference configuration of the continuum body with a smooth boundary $\Gamma = \Gamma_u \cup \Gamma_\sigma$. Here $\Gamma_u := \partial_u \Omega \subset \partial\Omega$ is the geometrical boundary, and $\Gamma_\sigma := \partial_\sigma \Omega \subset \partial\Omega$ is the kinetic boundary. The boundary conditions satisfy following conditions

$$\boldsymbol{u}|_{\Gamma_u} = \hat{\boldsymbol{u}} \ \ (\text{given}), \tag{4}$$

$$\boldsymbol{\sigma}|_{\Gamma_\sigma}\, \boldsymbol{n} = \hat{\boldsymbol{t}} \ \ (\text{given}), \tag{5}$$

where $\boldsymbol{t}$ is the traction, and $\boldsymbol{n}$ is the field normal to the boundary $\boldsymbol{\Gamma_\sigma}$.

Let Ω consist of *M* subdomains $\Omega^{(e)} \subset \Omega$ with the closed boundary $\Gamma^{(e)} := \partial\Omega^{(e)}$, as shown in Fig. 1., that is

$$\Omega = \bigcup_{e=1}^{M} \Omega^{(e)} \quad \text{here} \quad \Omega^{(r)} \cap \Omega^{(q)} = 0 \quad (r \neq q). \tag{6}$$

We denoted by $\Gamma_{<ab>}$ the common boundary for two subdomains $\Omega^{(a)}$ and $\Omega^{(b)}$ adjoined as shown in Fig. 2, and defined it as follows

$$\Gamma_{<ab>} \overset{\text{def.}}{=} \Gamma^{(a)} \cap \Gamma^{(b)}. \tag{7}$$

The relation for the displacement of $\boldsymbol{\Gamma}_{<ab>}$, which is the intersection boundary between $\Omega^{(a)}$ and $\Omega^{(b)}$, is as follows

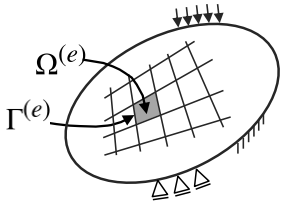

Fig. 1 Subdomain $\Omega^{(e)}$ and its common boundary $\Gamma^{(e)}$

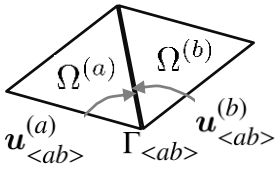

Fig. 2 Boundary $\boldsymbol{\Gamma}_{<ab>}$ between subdomain $\Omega^{(a)}$ and $\Omega^{(b)}$.

$$\boldsymbol{u}^{(a)}_{<ab>} = \boldsymbol{u}^{(b)}_{<ab>} \quad \text{on } \Gamma_{<ab>}. \tag{8}$$

This introduces a subsidiary condition into the framework of the virtual work equation with the Lagrange multiplier $\boldsymbol{\lambda}$ as follows

$$H_{ab} \overset{\text{def.}}{=} \delta \int_{\Gamma_{<ab>}} \boldsymbol{\lambda}\cdot(\boldsymbol{u}^{(a)}_{<ab>} - \boldsymbol{u}^{(b)}_{<ab>})\, dS, \tag{9}$$

where $\delta(\bullet)$ shows the variation of $(\bullet)$. From the above, the following hybrid-type virtual work equation is obtained

$$\sum_{e=1}^{M}\left(\int_{\Omega^{(e)}} \boldsymbol{\sigma}:\mathrm{grad}(\delta\boldsymbol{u})dV - \int_{\Omega^{(e)}} \boldsymbol{f}\cdot\delta\boldsymbol{u}\, dV\right)$$
$$-\sum_{s=1}^{N}\left(\delta\int_{\Gamma_{<s>}} \boldsymbol{\lambda}\cdot(\boldsymbol{u}^{(s_a)}_{<s>} - \boldsymbol{u}^{(s_b)}_{<s>})\, dS\right) - \int_{\Gamma_\sigma} \hat{\boldsymbol{t}}\cdot\delta\boldsymbol{u}\, dS = 0 \qquad {}^{\forall}\delta\boldsymbol{u}. \tag{10}$$

Here, *N* shows the number of common boundaries of the subdomain, and $\delta\boldsymbol{u}$ shows the virtual displacement. The superscripts (s_a) and (s_b) indicate the subdomains $\Omega^{(s_a)}$ and $\Omega^{(s_b)}$ related to the common boundary $\Gamma_{<s>}$.

2.2 Physical interpretation of Lagrange multiplier

The physical meaning of the Lagrange multiplier $\boldsymbol{\lambda}$ can be considered as a surface force at the boundary $\Gamma_{<s>}$ as in the following equation

$$\boldsymbol{\lambda} = \boldsymbol{t}^{(s_a)}(\boldsymbol{u}^{(s_a)}_{<s>}) = -\boldsymbol{t}^{(s_b)}(\boldsymbol{u}^{(s_b)}_{<s>}), \tag{11}$$

where $\boldsymbol{t}^{(s_a)}$ and $\boldsymbol{t}^{(s_b)}$ are surface forces at the boundary $\Gamma_{<s>}$ on the subdomains $\Omega^{(s_a)}$ and $\Omega^{(s_b)}$, respectively. In this paper, the Lagrange multiplier $\boldsymbol{\lambda}_{<ab>}$ on the boundary $\Gamma_{<ab>}$ is defined as follows

$$\boldsymbol{\lambda}_{<ab>} = \boldsymbol{k}\cdot\boldsymbol{\delta}_{<ab>}. \tag{12}$$

Here, $\delta_{<ab>}$ shows the relative displacement on the boundary $\Gamma_{<ab>}$, and $\boldsymbol{k}$ is the penalty function.

In the case of a two-dimensional problem, Eq. (12) is as follows

$$\begin{Bmatrix} \lambda_{n<ab>} \\ \lambda_{t<ab>} \end{Bmatrix} = \begin{bmatrix} k_n & 0 \\ 0 & k_t \end{bmatrix} \begin{Bmatrix} \delta_{n<ab>} \\ \delta_{t<ab>} \end{Bmatrix}, \tag{13}$$

where, $\delta_{n<ab>}$ and $\delta_{t<ab>}$ are the relative displacements in the normal tangential directions, respectively, to the boundary $\Gamma_{<ab>}$. Similarly, $\lambda_{n<ab>}$ and $\lambda_{t<ab>}$ are Lagrange multipliers in the

normal and tangential directions of the surface forces. The HPM can be described as follows by the penalty function p using the coefficient $\boldsymbol{k}$

$$k_n = k_t = p. \tag{14}$$

The penalty concept is the same as in discontinuous deformation analysis (DDA) which was developed by Shi and Goodman (1989), Sasaki *et al*. (1994). However, representation of contact behavior is different between DDA and HPM. DDA represents contact at a point, whereas HPM represents contact distributed on the boundary surface.

The subsidiary condition shown in Eq. (9) is transformable to a local coordinate system along the intersection boundary as follows

$$\boldsymbol{R}_{<ab>}\boldsymbol{u}^{(a)}_{<ab>} = \boldsymbol{R}_{<ab>}\boldsymbol{u}^{(b)}_{<ab>} \quad \text{on} \quad \Gamma_{<ab>}. \tag{15}$$

Here, $\boldsymbol{R}^{(a)}_{<ab>}$ and $\boldsymbol{R}^{(b)}_{<ab>}$ are the geometric transformations of each subdomain on the common boundary $\Gamma_{<ab>}$ related to the subdomain $\Omega^{(a)}$ and $\Omega^{(b)}$, respectively. The relation between these transformation matrices is as follows

$$-\boldsymbol{R}^{(a)}_{<ab>} = \boldsymbol{R}^{(b)}_{<ab>}. \tag{16}$$

Therefore, the relative displacement of a local coordinate system along the intersection boundary is obtained as follows

$$\boldsymbol{\delta}_{<ab>} = \boldsymbol{R}^{(a)}_{<ab>}\boldsymbol{u}^{(a)}_{<ab>} + \boldsymbol{R}^{(b)}_{<ab>}\boldsymbol{u}^{(b)}_{<ab>} = \sum_{l=1}^{2} \boldsymbol{R}^{(l)}_{<ab>}\boldsymbol{u}^{(l)}_{<ab>}. \tag{17}$$

Substituting Eq. (17) into Eq. (9), we can obtain the following equation

$$H_{ab} = -\delta \int_{\Gamma_{<ab>}} \boldsymbol{\lambda}^{t}_{<ab>}\boldsymbol{\delta}_{<ab>}\, dS = -\delta \int_{\Gamma_{<ab>}} \boldsymbol{\delta}^{t}_{<ab>}\boldsymbol{k}\, \boldsymbol{\delta}_{<ab>}\, dS. \tag{18}$$

2.3 Discretized equation by matrix form

The independent linear displacement field $\boldsymbol{u}^{(e)}$ in each subdomain $\Omega^{(e)}$ is assumed as follows

$$\boldsymbol{u}^{(e)} = \boldsymbol{N}^{(e)}_{d}\boldsymbol{d}^{(e)} + \boldsymbol{N}^{(e)}_{\varepsilon}\boldsymbol{\varepsilon}^{(e)}. \tag{19}$$

Here, $\boldsymbol{d}^{(e)}$ shows the rigid displacement and the rigid rotation at point $\boldsymbol{x}^p = (x_p, y_p) \in \Omega^{(e)}$, and $\boldsymbol{\varepsilon}^{(e)}$ shows a constant strain in the subdomain $\Omega^{(e)}$.

In the case of a two-dimensional problem, the coefficient in Eq. (19) is as follows:

$$\boldsymbol{d}^{(e)} = \lfloor u^p, v^p, \theta^p \rfloor^t \ , \ \boldsymbol{\varepsilon}^{(e)} = \lfloor \varepsilon_x, \varepsilon_y, \gamma_{xy} \rfloor^t,$$

$$\boldsymbol{N}^{(e)}_{d} = \begin{bmatrix} 1 & 0 & -(y-y_p) \\ 0 & 1 & (x-x_p) \end{bmatrix}, \ \boldsymbol{N}^{(e)}_{\varepsilon} = \begin{bmatrix} x-x_p & 0 & (y-y_p)/2 \\ 0 & y-y_p & (x-x_p)/2 \end{bmatrix}.$$

Hear, u^p and v^p indicate rigid displacement at the point $\boldsymbol{x}^p$ in a subdomain, θ^p indicates rigid rotation, and ε_x, ε_y, and γ_{xy} indicate constant strain in a subdomain. In the present paper, Eq. (19) is applied for a linear displacement field. In the case of a high-order displacement field, a high-order term is added to Eq. (19).

For the displacement field used in the present paper, the degrees of freedom are the rigid displacement and strain at the arbitrary point in the subdomain. The displacement field is

expressed in this model using the parameter for an arbitrary point in each subdomain, so that the displacement is not defined by the node as in the displacement model of FEM. Therefore, an arbitrary polygon, a polyhedron, or a curved surface body can be used as subdomain without limiting the element shape.

We rewrite the Eq. (10) in matrix form for discretization of the hybrid-type virtual work equation

$$\sum_{e=1}^{M}\left(\int_{\Omega^{(e)}}[\boldsymbol{L}\delta\boldsymbol{u}]^t\boldsymbol{D}[\boldsymbol{L}\boldsymbol{u}]\,dV-\int_{\Omega^{(e)}}\delta\boldsymbol{u}^t\boldsymbol{f}\,dV-\int_{\Gamma_\sigma}\delta\boldsymbol{u}^t\hat{\boldsymbol{t}}\,dS\right)-\sum_{s=1}^{N}\left(\delta\int_{\Gamma_{<s>}}\boldsymbol{\delta}^t\boldsymbol{k}\boldsymbol{\delta}\,dS\right)=0. \quad (20)$$

Here, $\boldsymbol{L}$ is a matrix of a differentiation operator. The displacement field of the Eq. (19) and virtual displacement are written simply as follows

$$\boldsymbol{u}^{(e)}=\boldsymbol{N}^{(e)}\boldsymbol{U}^{(e)}, \text{ where } \boldsymbol{U}^{(e)}=\lfloor\boldsymbol{d}^{(e)},\boldsymbol{\varepsilon}^{(e)}\rfloor^t,\ \boldsymbol{N}^{(e)}=\lfloor\boldsymbol{N}_d^{(e)},\boldsymbol{N}_\varepsilon^{(e)}\rfloor, \quad (21)$$

$$\delta\boldsymbol{u}^{(e)}=\boldsymbol{N}^{(e)}\delta\boldsymbol{U}^{(e)}, \text{ where } \delta\boldsymbol{U}^{(e)}=\lfloor\delta\boldsymbol{d}^{(e)},\delta\boldsymbol{\varepsilon}^{(e)}\rfloor^t. \quad (22)$$

Consequently, we obtain following equation

$$\boldsymbol{L}\boldsymbol{u}^{(e)}=\boldsymbol{L}\boldsymbol{N}^{(e)}\boldsymbol{U}^{(e)}=\boldsymbol{B}^{(e)}\boldsymbol{U}^{(e)}, \text{ where } \boldsymbol{B}^{(e)}=\boldsymbol{L}\boldsymbol{N}^{(e)}. \quad (23)$$

However, the relative displacement $\boldsymbol{\delta}_{<ab>}$ is described as follows

$$\boldsymbol{\delta}_{<ab>}=\boldsymbol{B}_{<ab>}\boldsymbol{U}_{<ab>}, \quad (24)$$

where, $\boldsymbol{B}_{<ab>}=\lfloor\boldsymbol{R}^{(a)}_{<ab>}\boldsymbol{N}^{(a)}\ ,\ \boldsymbol{R}^{(b)}_{<ab>}\boldsymbol{N}^{(b)}\rfloor$, and $\boldsymbol{U}_{<ab>}=\lfloor\boldsymbol{U}^{(a)}\ ,\ \boldsymbol{U}^{(b)}\rfloor^t$.

The discretized equation by substituting the above-mentioned relations in Eq. (20) is obtained as follows

$$\delta\boldsymbol{U}^t\left(\sum_{e=1}^{M}\boldsymbol{K}^{(e)}+\sum_{s=1}^{N}\boldsymbol{K}_{<s>}\right)\boldsymbol{U}-\delta\boldsymbol{U}^t\left(\sum_{e=1}^{M}\boldsymbol{P}^{(e)}\right)=0, \quad (25)$$

where,

$$\boldsymbol{K}^{(e)}=\int_{\Omega^{(e)}}(\boldsymbol{B}^{(e)})^t\boldsymbol{D}^{(e)}\boldsymbol{B}^{(e)}\,dV,$$

$$\boldsymbol{K}_{<s>}=\int_{\Gamma_{<s>}}\boldsymbol{B}^t_{<s>}\boldsymbol{k}\boldsymbol{B}_{<s>}\,dS,$$

$$\boldsymbol{P}^{(e)}=\int_{\Omega^{(e)}}(\boldsymbol{N}^{(e)})^t\boldsymbol{f}\,dV+\int_{\Gamma_\sigma}(\boldsymbol{N}^{(e)})^t\,\hat{\boldsymbol{t}}\,dS.$$

Since the virtual displacement $\delta\boldsymbol{U}$ of Eq. (25) is arbitrary, we obtain the following discretized equation

$$\boldsymbol{K}\boldsymbol{U}=\boldsymbol{P}, \quad (26)$$

where,

$$\boldsymbol{K}=\sum_{e=1}^{M}\boldsymbol{K}^{(e)}+\sum_{s=1}^{N}\boldsymbol{K}_{<s>},$$

$$\boldsymbol{P}=\sum_{e=1}^{M}\boldsymbol{P}^{(e)}.$$

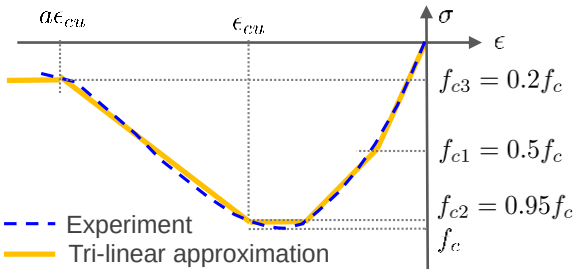

Fig. 3 The skeleton curve of compressive stress

As described above, the discretized equation of the HPM becomes the simultaneous linear equation of Eq. (26). The coefficient matrix of $\boldsymbol{K}$ on the left-hand side can be obtained to assemble each stiffness matrix of the subdomain and subsidiary condition on the boundary. The discontinuous phenomena of opening, etc., can be expressed without changing the degrees of freedom by setting the value of Eq. (12) to zero.

3. Implementation of the constitutive model of concrete material

A typical constitutive model of concrete material is generally based on an empirical formula obtained from many experiments. For example, a smeared crack model, which is generally used in FEM, uses a local coordinate system with normal and tangential directions set relative to the crack after crack initiation. The concrete stress is calculated using an empirical formula obtained from uniaxial experimental tests. Before applying an empirical formula, the stress tensor is rotated by a translation matrix, which is determined by the direction of the crack.

The empirical formula for concrete is implemented in the HPM as well as the FEM. However, as mentioned above, the degrees of freedom are different from the FEM. In the FEM, the strain and stress are evaluated at Gaussian integration points. However, in the HPM, the tensile failure of concrete is evaluated at the boundary of the subdomain, and compressive failure is evaluated within the subdomain. Tensile failure, namely, a discrete crack, is represented by the separation of two subdomains at a boundary. The constitutive model of tensile failure is represented by the relationship between tensile stress and relative displacement at the intersection boundary between two subdomains. This concept is the same with the cohesive crack model. Here, we explain the constitutive model of concrete for tensile stress and compressive stress implemented in the HPM for a plane stress problem. The problem of a constant-strain triangle element under plane stress is used here. The degrees of freedom are defined at the centroid of a triangle element.

3.1 Constitutive law for compressive stress

A constitutive model can be based on a hardening rule and a yield surface in a stress space derived by experiment. First, we describe the hardening rule. The dashed line of Fig. 3 shows a typical compressive stress-strain relationship for concrete. The minimum stress of this curve indicates the compressive strength f_c. The stiffness degrades gradually during increasing stress until f_c. After the stress exceeds f_c, softening phenomena take place until ultimate strain. The solid line in Fig. 3 shows a tri-linear approximation for the skeleton curve, which was also adopted in

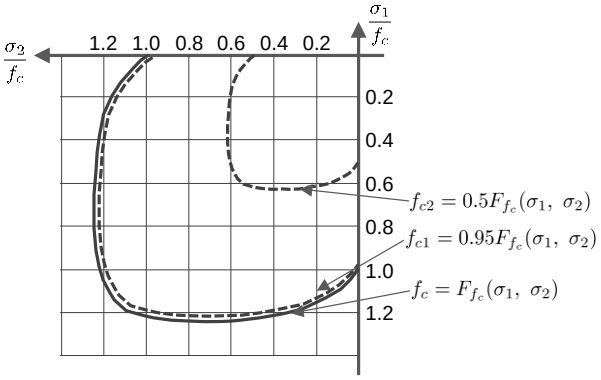

Fig. 4 Yield surface under biaxial stress

the RBSM by Takeuchi *et al.* (2005). The first degrading point of the skeleton curve is designated as the first compressive yield stress f_{c1} whose value is defined as 50% of the f_c value. After f_{c1}, the tangential stiffness is set to 50% of the initial stiffness value. The second degrading point, namely the second compressive yield stress f_{c2}, is defined as 95% of the f_c value because if the f_c value is used for the second degrading point, the second tangential stiffness is less than the actual value. After f_{c2}, the tangential stiffness is set to zero until the ultimate compressive strain ε_{cu}. After ε_{cu}, the stress is released until the strain equals $a \times \varepsilon_{cu}$, where a is the coefficient depending on the material. When the relative displacement is greater than $a\varepsilon_{cu}$, the stress is kept to a value of 0.2 f_c.

The compressive strength f_c changes with the transition of the stress under biaxial stress states. A yield surface under various biaxial stress states was proposed by Kupfer *et al.* (1969) as shown in Fig. 4 (solid line). It can be expressed as $f_c = F_{f_c}(\sigma_1,\ \sigma_2)$, where f_c is defined by the principal stresses σ_1 and σ_2. This yield surface is adopted in this paper.

When f_{c1} and f_{c2} are defined by $f_{c1} = 0.5f_c$ and $f_{c2} = 0.95f_c$ as the yield surface $f_c = F_{f_c}(\sigma_1,\ \sigma_2)$, the surfaces of the degrading points f_{c1} and f_{c2} are shown in Fig. 4 with dashed lines. The tangential Young's modulus E_T is determined by the position in Fig. 4 under the current principal stresses σ_1 and σ_2. The incremental stresses are calculated with the following equation

$$d\boldsymbol{\sigma} = \boldsymbol{D}^{ep} d\boldsymbol{\varepsilon}, \tag{27}$$

where $d\boldsymbol{\sigma}$, $d\boldsymbol{\varepsilon}$, and $\boldsymbol{D}^{ep}$ are the incremental stress, incremental strain, and stress-stain relationship matrix, respectively. $\boldsymbol{D}^{ep}$ is defined as

$$\boldsymbol{D}^{ep} = \frac{E_T}{1-\nu^2}\begin{bmatrix} 1 & \nu & 0 \\ \nu & 1 & 0 \\ 0 & 0 & \frac{1-\nu}{2} \end{bmatrix}, \tag{28}$$

where E_T and ν are the tangential Young's modulus and Poisson's ratio, respectively. In Eq. (27), axial and shear stiffness are degraded with the same ratio that assumes a constant Poisson's ratio.

The origin-oriented model was adopted for hysteresis behavior. The stress and strain behavior of the method is shown in Fig. 5. When strain is reversed during the loading process on the skeleton curve such as at the point *C* or *E* in Fig. 5, it has a linear behavior on a straight line oriented to origin point *O*. When the strain is greater than the maximum reversal point, it returns to

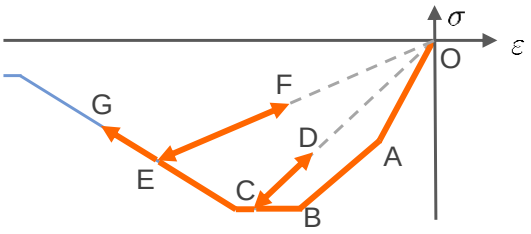

Fig. 5 The hysteresis rule in compressive stress

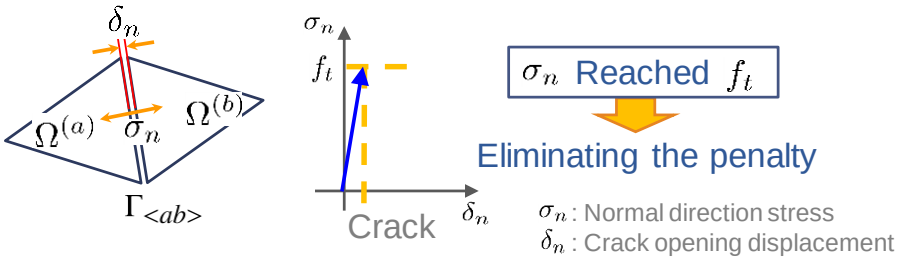

Fig. 6 Surface force and tensile strength

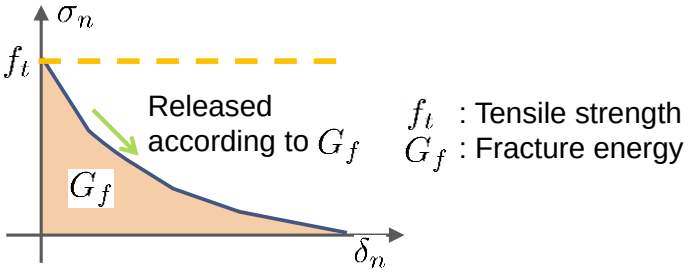

Fig. 7 The tension softening curve for concrete

the skeleton curve. The incremental stress $d\sigma$ is calculated by Eq. (27) using the tangential stiffness E_T which is obtained from the slope of this straight line.

3.2. A constitutive law for tensile stress

The HPM is capable of separating two subdomains by simply eliminating the penalty. This feature is suitable for representing a discrete crack in the concrete. When the surface force σ_n at the boundary $\mathbf{\Gamma}_{<ab>}$ reaches tensile failure strength f_t, we can then eliminate the penalty and compute the discrete crack as shown in Fig. 6.

The stress in the concrete decreases gradually with the progress of the crack opening displacement after exceeded tensile failure. This behavior is called tension softening. Concrete is considered as a quasi-brittle material compared with a brittle material such as glass. Hilerborg *et al.* (1976) introduced fracture energy for this tensile softening behavior in the fictitious (or cohesive) crack model. The fracture energy G_f is the area enclosed by the tension softening curve and has a unique value representing the strength of concrete material with a tensile strength f_t. In

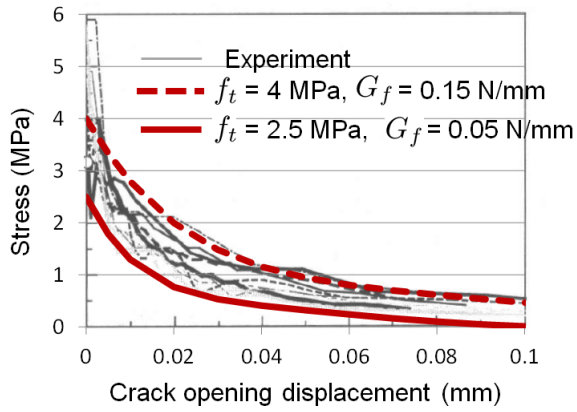

Fig. 8 The test results of tension softening curve (after JCI 2001)

the HPM, the tension softening curve is defined as shown in Fig. 7 as the relation between the normal-direction stress σ_n and crack opening displacement σ_n .

Many tests have been conducted by many institutes and universities in order to obtain the tension softening curve and fracture energy G_f. In a Research Committee report on fracture mechanics test methods for concrete by the Japan Concrete Institute (JCI) (2001), the French International Union of Laboratories and Experts in Construction Materials, Systems, and Structures (RILEM) has recommended a test method to obtain fracture energy based on a three-point bending test of a notched beam. Several institutes and universities have reported results of round-robin tests with this method. The black lines in Fig. 8 show the results of these tests. In the HPM, we apply a tension-softening curve which corresponds to these test results.

Nakamura *et al.* (1999) compared many empirical derivations of the tension-softening curve in their paper. It was determined that the empirical expression by Hordijk *et al.* (1986) (Eq. (29)) was well matched with past experiments, and they used this expression as a standard for comparison

$$\frac{\sigma}{f_t} = \left(1 + 27\left(\frac{w}{w_c}\right)^3\right) exp\left(-6.93\frac{w}{w_c}\right) - 28\frac{w}{w_c} exp\,(-6.93), \tag{29}$$

where w_c, the limited virtual crack opening displacement (mm) when the tensile stress is zero, is given by

$$w_c = 5.14 G_f / f_t, \tag{30}$$

where f_t is the tensile strength (MPa), and G_f is the fracture energy (N/mm).

Eq. (29) is adopted for the tension-softening curve in the present paper since it corresponds better to the test results than other proposed empirical expressions. Eq. (29) uses the limited virtual crack displacement w_c which is the crack displacement when the tensile stress is zero. It is practical and useful for code to be able to change the status of failure after w_c.

The red lines in Fig. 8 shows examples of tension softening curves using Eq. (29). The red dashed line shows the curve for a tensile strength f_t=4.0 MPa and fracture energy G_f=0.15 N/mm, and the red solid line is f_t=2.5 MPa and G_f=0.05 N/mm. The test results are almost all within these two lines. Therefore Eq. (29) is capable of representing various materials in concrete. According to this committee report, the average value of the fracture energy in these tests was 0.141 (N/mm).

The origin-oriented model is used for hysteresis behavior of tensile stress as well as

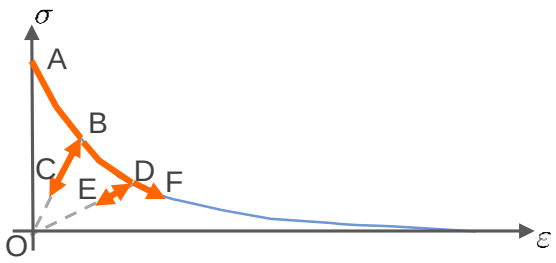

Fig. 9 The hysteresis rule in tensile stress

compressive stress. When the relative displacement δ_n is reversed in the tension softening curve as shown at point B or D in Fig. 9 for the maximum tensile strain, it has linear behavior on a straight line that is oriented toward origin O. When it exceeds the maximum tensile strain, it returns to the skeleton curve, e.g., along the path E-D-F in Fig. 9.

In this way, after crack initiation, accurate stress and displacement can be calculated because the fracture energy is determined directly.

However, the location of the discrete crack depends on the division of the mesh. There is an error due to the difference in the exact crack location. To correct this error, the division of the mesh can be changed by predicting of the location of the crack, or a finer mesh can be used.

4. Validation

To validate the HPM with a newly implemented concrete constitutive model, an anchor bolt pullout test which shows typical progressive failure was simulated.

4.1 Description of an anchor bolt pullout test

The crack model was implemented in the HPM to solve a progressive failure problem. This was validated by a simulation of an anchor bolt pullout test. The details of this experiment are reported in "Application of fracture mechanics to concrete structures" (1993) which was carried out by the "Committee of fracture mechanics applied research" of the JCI. The anchor bolt pullout test is one of the round robin tests.

Two specimens were tested. The first specimen (Model #1) was the same as that used in common tests conducted by RILEM (1991). The second specimen (Model #2) was the same as the test specimen used by Lun (1990) who experimentally confirmed the progressive crack and fracture mechanisms by laser speckle.

The schematic test model is shown in Fig. 10. The anchor bolt is embedded in a flat concrete block. The size of Model #1 was l=900 mm, thickness b=100 mm, Model #2 was less than half the size of Model #1 with l=350 mm, b=80 mm. The embedded depth of the anchor bolt was d=150 mm in Model #1 and d=60 mm in Model #2.

The embedded anchor bolt was pulled up while the concrete block was held down by the two support bars. A lifting force was applied to the top of the anchor bolt. The ratios of the distances from the supported point to anchor bolt a divided by the sizes of concrete blocks l were 0.33 in Model #1 and 0.17 in Model #2. This ratio for Model #1 was larger than for Model #2.

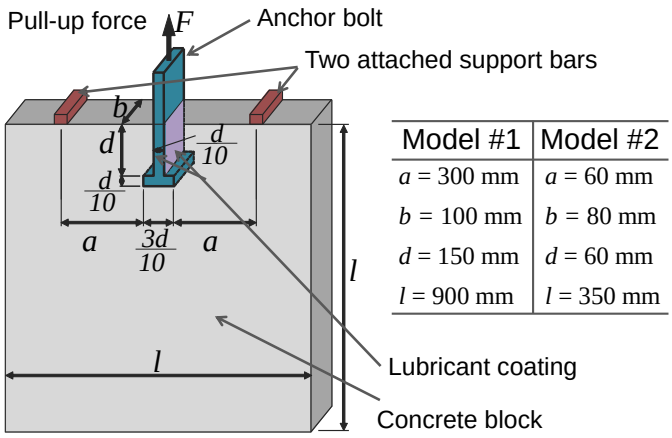

Model #1	Model #2
a = 300 mm	a = 60 mm
b = 100 mm	b = 80 mm
d = 150 mm	d = 60 mm
l = 900 mm	l = 350 mm

Fig. 10 Schematic of the test model

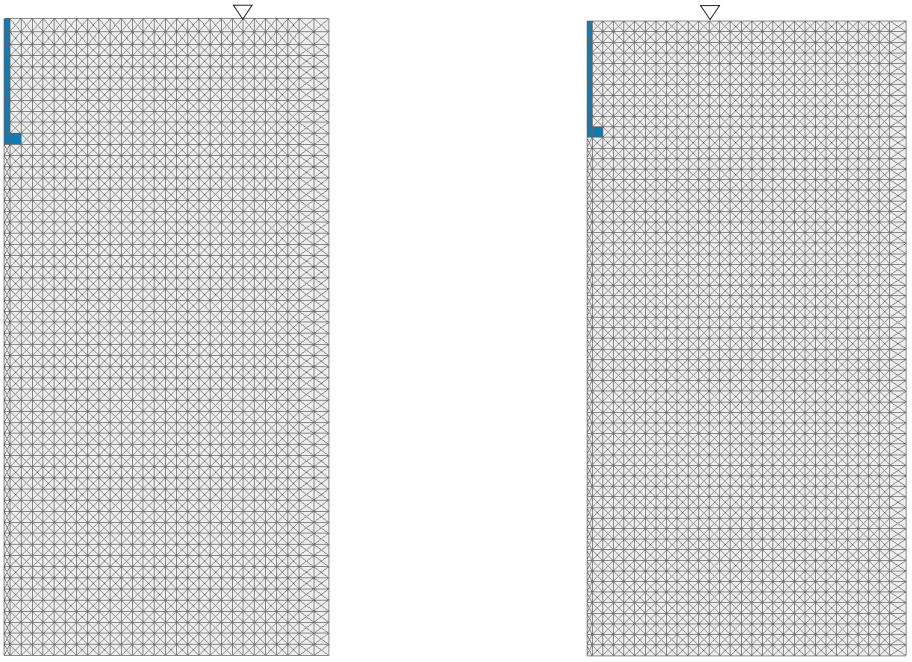

(a) Model #1 (b) Model #2

Fig. 11 Simulation model

Both side of the anchor are considered slippery because they are coated with lubricant.

4.2. Simulation model

Simulation models of Model #1 and #2 are shown in Fig. 11. We solved half of the experiment considering symmetry. On the left-hand side we applied symmetric boundary conditions. The supported points are indicated with triangle marks. Only the vertical direction was fixed, because

Table 1 Material properties
(a) Concrete

	Model #1	Model #2
Compressive strength f_c (MPa)	32.6	34.3
Tensile strength f_t (MPa)	2.8	3.4
Young's modulus E (MPa)	2.47×10^4	2.94×10^4
Poisson's ratio ν	0.167	0.167

(b) Anchor bolt

	Value
Young's modulus E (MPa)	2.059×10^5
Poisson's ratio ν	0.3

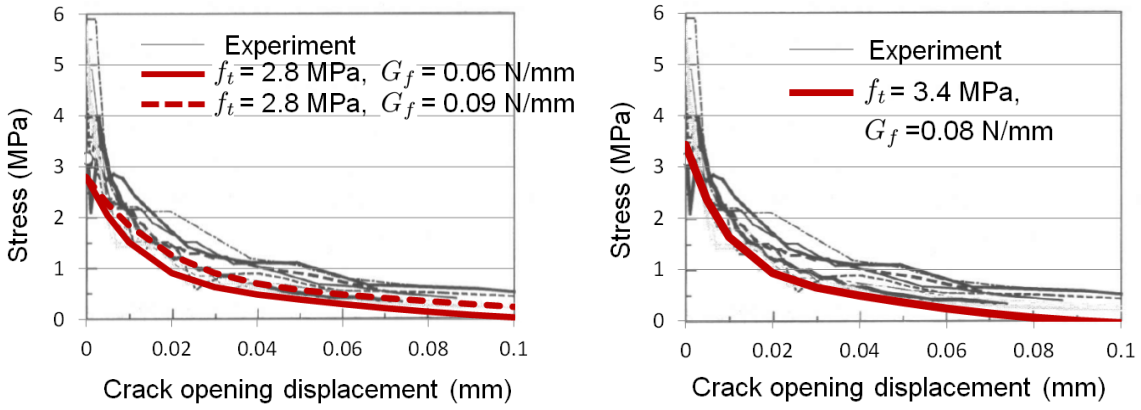

(a) Model #1 (b) Model #2

Fig. 12 The tension softening curve of the concrete

the concrete block could be rotated during the pullout test. The static load was applied to the top of the anchor bolt. The incremental load was divided into small values. The bottom and right side had free boundary conditions. The mesh size was chosen so a reasonable crack path could be obtained.

The material properties of the concrete and anchor bolt are shown in Table 1. These values were set according to the JCI report (1993). For Model #1 we used the material properties reported by participant T2-3 to compare with the results of the tests conducted by T2-3. The material properties of Model #2 were specified in advance before the test. The adhesion value at the side of the anchor bolt was specified as a small value of 0.01 MPa. The adhesion value at the anchorage zone was 14 MPa.

The tension softening curves that were used are shown in Fig. 12. Fig. 12(a) shows the tension softening curve for Model #1 which had a tensile strength f_t=3.4 MPa and a fracture energy G_f=0.06 or 0.09 N/mm. Fig. 12(b) shows the curve of Model #2 which had f_t=2.8 MPa and G_f=0.08 N/mm. As the tensile strengths in both curves are small compared to the test results, the tension softening curve was reduced by using a small G_f value.

Nonlinear algorithm is very important to accurately calculate the tensile cracking and compressive failure problem in concrete. Takeuchi's extended r_{min} method (2005) was suited for

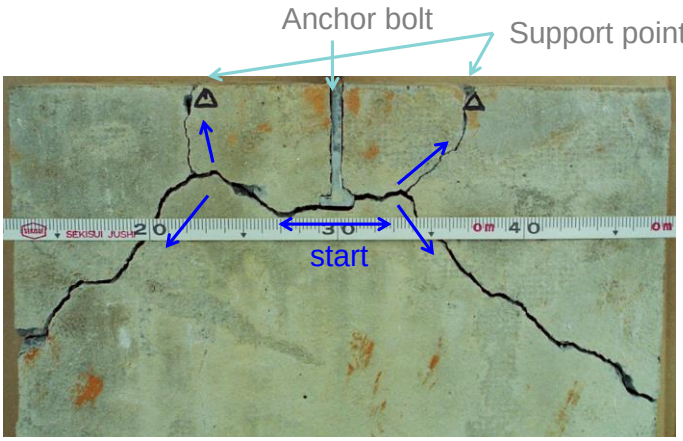

Fig. 13 Crack shape after the test

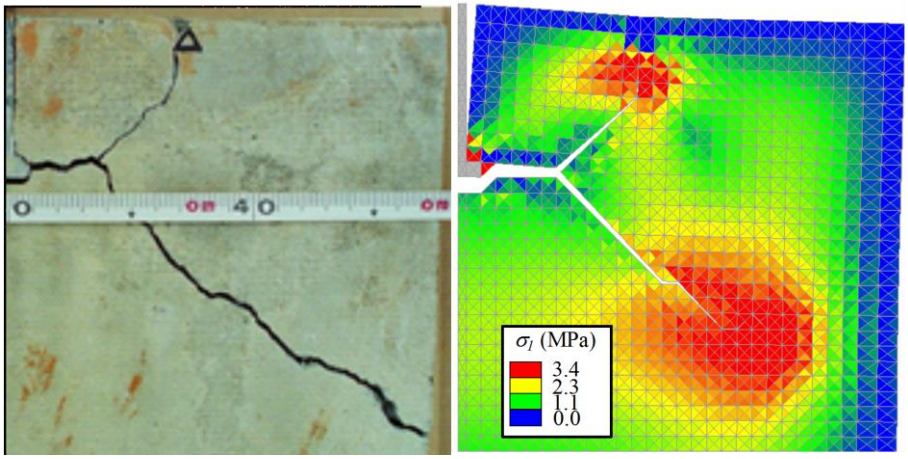

(a) Experiments (b) Analysis

Fig. 14 Comparison of crack patterns

this purpose and used in the presented paper, which was originated by Yamada (1968).

4.3 Numerical results

4.3.1 Results of Model #2

With Model #2, the propagation of the dominant crack can be recognized by the photograph which was taken after the experiments and shown in Fig. 13. Broken parts were set to their original shapes after the experiments. Cracks started from anchor tip and propagated to both sides. Interestingly, they diverged toward supported points and the side of concrete block. The crack shapes on both sides were nearly symmetric. We assumed this symmetry at our simulation.

Fig. 14 shows the crack pattern of Model #2. Fig. 14(a) shows the experimental result for the right half of Fig. 13. Fig. 14(b) shows the numerical deformation with an amplification factor of 20.0 for recognizing crack width. The contour shows the maximum principal stress σ_1.

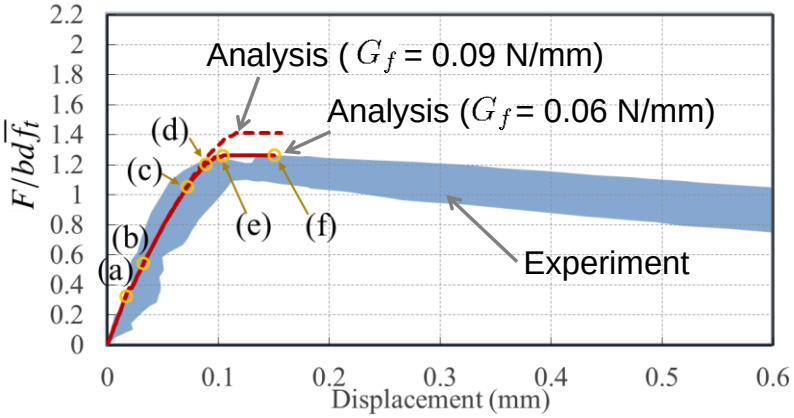

Fig. 15 Relationship between normalized load and displacement

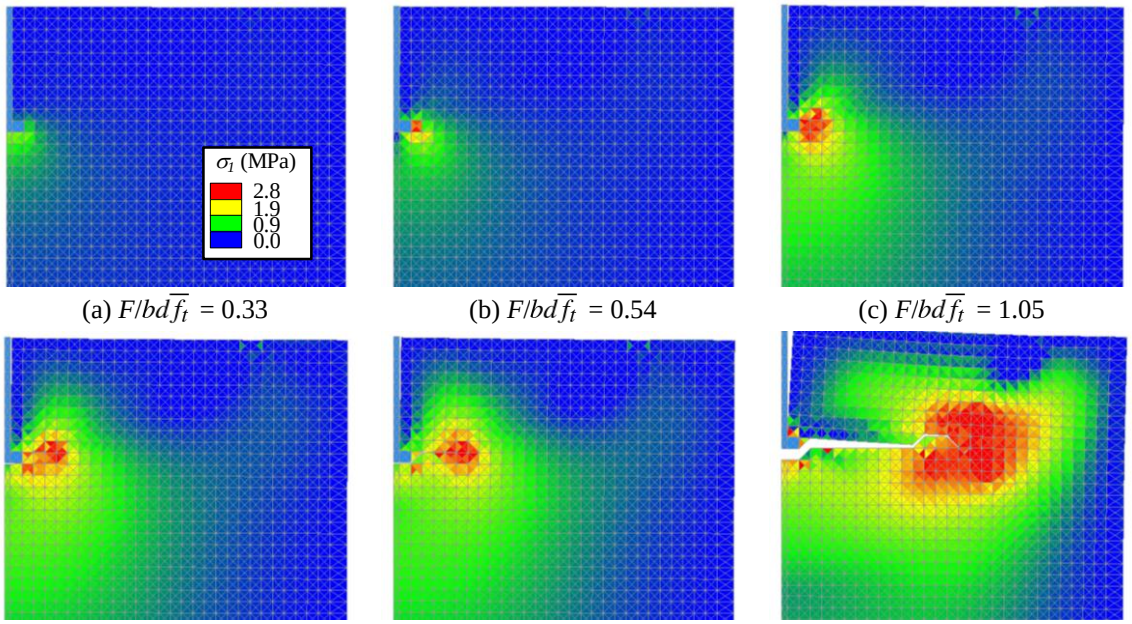

(a) $F/bd\overline{f_t}$ = 0.33 (b) $F/bd\overline{f_t}$ = 0.54 (c) $F/bd\overline{f_t}$ = 1.05

(d) $F/bd\overline{f_t}$ = 1.20 (e) $F/bd\overline{f_t}$ = 1.259 (f) $F/bd\overline{f_t}$ = 1.264

Fig. 16 Deformation and contour of maximum principal stress σ_1

At first, the crack initiated at the bottom of the anchor bolt and propagated to the left; then it branched in the upper and lower directions. The crack pattern was well matched with the experiment. The propagation of the progressive crack was well simulated. The red color of the σ_1 contour corresponds to tensile strength where the crack subsequently occurred. Concrete near tip of the crack was under concentrated stress as indicated by the red region of the contour shown in Fig. 14(b). These concentrated stresses can be represented by considering a discrete crack which is realized by separating the subdomains.

4.3.2 Results of Model #1

In the tests of Model #1, the results of the experimental tests were compared with the analysis using normalized force $F/bd\overline{f_t}$ to avoid the difference in compressive strength, where F is the subjected load, b is the thickness of the concrete block, d is embedded depth of the anchor bolt, and $\overline{f_t}$ is calculated by following equation

$$\overline{f_t} = 0.33\sqrt{f_c} \tag{31}$$

where f_c is the compressive strength (MPa).

Fig. 15 shows the relationship between the normalized force and crack displacement. The broad blue line shows the experimental results, and red lines show the numerical results. The solid line and dashed line show the results for G_f=0.06 and 0.09 N/mm, respectively. The result for G_f=0.06 N/mm was well matched with the experimental results.

Fig. 16 shows the transition of numerical deformation (amplification factor 50.0) with the contour of the maximum principal stress σ_1. The notation (a)-(f) corresponds to the yellow circle markers in Fig. 15. The initial slope of the curve, which is approximate, represents that the prediction of the deformation before the crack was accurate (Fig. 15(a)). The numerical result corresponds well to the experimental results after crack initiation (Fig. 15(b) and (c)). The relationship between normalized force and crack displacement was also accurately predicted during the process of dominant crack propagation (Figs. 15(d)-(f)).

We presented simulations of two anchor bolt pullout tests with the proposed HPM, which is applicable to a flat concrete structure. In Model #1, the quantitative validation was confirmed. The numerical result of relationship between normalized force and displacement was well matched with the experimental result. In Model #2, qualitative validation was also confirmed. The crack shape in the numerical result was well matched with the experimental result.

5. Conclusions

A method to simulate progressive concrete failure was presented and proved by performing experimental tests. The presented method is an extension of the hybrid-type penalty method (HPM) with a constitutive model (discrete crack model) for concrete. The discrete crack is evaluated at the intersection boundary between subdomains of HPM. Nonlinearity of compressive behavior is considered in the compressive stress-strain components of the subdomain of HPM based on the tri-linear approximation function of an empirical stress-strain relationship. In the intersection boundary of the subdomain, it is easy to simulate the tensile stress behavior and crack displacement using the empirical expressions which were introduced by Hordijk *et al.* (1986).

To confirm the validity of the new HPM, we carried out simulations of anchor bolt pullout tests. First, the pullout strength was compared in the test Model #1, and we obtained good agreement in the relationship between force and displacement. Secondary the progressive crack was compared with the observed record of the test Model #2. The tip and branch of the crack corresponded well to the test results. These agreements with the qualitative and quantitative simulation proved the correctness of the proposed numerical method.

It is important that the method is able to simulate flat concrete. More complicated problems such as failure of reinforced concrete can be solved based on the method proposed here. In the future we shall extend the method to evaluate failure phenomena of reinforced concrete.

Acknowledgments

The experimental results in Fig. 8, Fig. 12, and Fig. 15 were published in the Committee Report of Japan Concrete Institute (JCI).

Special thanks to Dr. Ueda who is teaching the authors carefully about discrete limit analysis and the constitutive model of concrete.

References

Barenblatt, G.I. (1962), "The mathematical theory of equilibrium cracks in brittle fracture", *Adv. Appl. Fract.*, **7**, 55-129.

Bazant, Z.P. and Oh, B.H. (1983), "Crack band theory for fracture in concrete", *Mater. Struct.*, **16**, 155-177.

Belytschko, T.T. and Black, T. (1999), "Elastic crack growth in finite elements with minimal remeshing", *Int. J. Numer. Meth. Eng.*, **45**(5), 601-620.

Cornelissen, H.A.W., Hordijk, D.A. and Reinhardt, H.W. (1986), "Experiments and theory for the application of fracture mechanics to normal and lightweight concrete", *Int. Conf. on Fracture Mechanics of Concrete*, Ed. Wittmann, F.H., Elsevier, Amsterdam.

Gedik, Y.H., Nakamura, H., Yamamoto, Y. and Kunieda, M. (2011), "Evaluation of three-dimensional effects in short deep beams using a rigid-body-spring-model", *Cement Concrete Compos.*, **33**(9-10), 978-91.

Hillerborg, A., Modéer, M. and Petersson, P.E. (1976), "Analysis of crack formation and crack growth in concrete by means of fracture mechanics and finite elements", *Cement Concrete Res.*, **6**, 773-782.

JCI (1993), Application of Fracture Mechanics to Concrete Structures.

Kawai, T. (1977), "New element models in discrete structural analysis", *J. Soc. Nav. Arch. JPN*, **141**, 187-193.

Kitsutaka, Y., Uchida, Y., Kaneko, Y. and Kanda, T. (2001), "Report of research committee on testing method of fracture properties of concrete", *Proceedings of the Japan Concrete Institute*, **23**(1). (in Japanese)

Kupfer, H., Hilsdorf, H.K. and Rüsch, H. (1969), "Behavior of concrete under biaxial stresses", *ACI J.*, **66**(66-8), 656-666.

Lun, C.C. (1990), "Observation of crack growth from anchor bolt by laser speckle method and application of fracture mechanics", Master Thesis of Asian Institute of Technology, March.

Miehe, C. and Gürses, E. (2007), "A robust algorithm for configurational-force-driven brittle crack propagation with R-adaptive mesh alignment", *Int. J. Numer. Meth. Eng.*, **72**, 127-155.

Nakamura, S., Kitsutake, Y., Mihashi, H. and Uchida, Y. (1999), "Discussion on standard evaluation method for tension softening properties of concrete", *Concrete Res. Tech.*, **10**(1), 151-164. (in Japanese)

RILEM TC90-FMA (1991), "Committee on applications of fracture mechanics of concrete-round-robin analysis of anchor bolts", Preliminary Report.

Rice, J.R. (1968), "Path independent integral and the approximate analysis of strain consideration by notches and cracks", *J. Appl. Mech.*, **35**, 379-386.

Rabczuk, T. and Belytschko, T. (2007), "A three-dimensional large deformation meshfree method for arbitrary evolving cracks", *Comput. Meth. Appl. Mech. Eng.*, **196**, 2777-2779.

Sasaki, T., Ohnishi, Y. and Yoshinaka, R. (1994), "Discontinuous deformation analysis and its application to rock mechanics problems", *JSCE*, **493**(III-27), 11-20. (in Japanese)

Sato, Y. and Naganuma, K. (2007), "Discrete-like crack simulation by smeared crack-based FEM for reinforced concrete", *Earthq. Eng. Struct. Dyn.*, **36**, 2137-2152.

Shi, G.H. and Goodman, R.E. (1989), "Generalization of two-dimensional discontinuous deformation analysis for forward modeling", *Int. J. Numer. Anal. Meth. Geomech.*, **13**, 359-380.

Takeuchi, N. (1991), "Discrete limit analysis in soil mechanics", Baifukan. (in Japanese)

Takeuchi, N., Kusabuka, M., Takeda, H., Sato, K. and Kawai, T. (2000), "The discrete limit analysis by

using the hybrid model with the penalty", *JSCE*, **46A**, 261-270. (in Japanese)
Takeuchi, N., Ohki, H., Kambayashi, A. and Kusabuka, M. (2001), "Material non-linear analysis by using discrete model applied penalty method in hybrid displacement model", *Tran. JSCES*, Paper No. 20010002, 53-62. (in Japanese)
Takeuchi, N., Ueda, M., Kambayashi, A. and Kito, H. (2005), *Discrete Limit Analysis of Reinforced Concrete Structure*, Maruzen, Tokyo.
Theiner, Y. and Hofstetter, G. (2009), "Numerical prediction of crack propagation and crack widths in concrete structures", *Eng. Struct.*, **31**(8), 1832-40.
Unger, J. F., Eckardt, S. and Könke, C. (2007), "Modelling of cohesive crack growth in concrete structures with the extended finite element method", *Comput. Meth. Appl. Mech. Eng.*, **196**(41-44), 4087-4100.
Yamada, Y., Yoshimura, N. and Sakurai, T. (1968), "Plastic stress-strain matrix and its application for the solution of elasto-plastic problem by a finite element method", *Int. J. Mech. Sci.*, **10**, 343-354.

CC